IEEE Robotics and Automation Letters (RA-L) paper, presented at ICRA 2026, Vienna, Austria. Cite as RA-L paper.

Active Learning Design: Modeling Force Output for Axisymmetric Soft Pneumatic Actuators

Gregory M. Campbell[1], Gentian Muhaxheri[2], Leonardo Ferreira Guilhoto[1], Christian D. Santangelo[2], Paris Perdikaris[1], James Pikul[3], and Mark Yim[1]

***Abstract*—Soft pneumatic actuators (SPA) made from elastomeric materials can provide large strain and large force. The behavior of locally strain-restricted hyperelastic materials under inflation has been investigated thoroughly for shape reconfiguration, but requires further investigation for trajectories involving external force. In this work we model force-pressure-height relationships for a concentrically strain-limited class of soft pneumatic actuators and demonstrate the use of this model to design SPA response for object lifting. We predict relationships under different loadings by solving energy minimization equations and verify this theory by using an automated test rig to collect rich data for n=22 Ecoflex 00-30 membranes. We collect data using an active learning pipeline to efficiently model the design space. We show that this learned model outperforms the theory-based model and a naive regression. We use our model to optimize membrane design for different lift tasks and compare this performance to other designs. These contributions represent a step towards understanding the natural response for this class of actuator and embodying intelligent lifts in a single-pressure input actuator system.**

***Index Terms*—Soft Robot Materials and Design; Hydraulic/Pneumatic Actuators; Modeling, Control, and Learning for Soft Robots; Active Learning; Hyperelastic Rubbers**

I. Introduction

SOFT actuators are promising for physical human-robot interaction in part due to their compliance. Control of a soft pneumatic robot requires careful characterization of its fluidic elastomer actuators and the elements that supply fluid energy to predict these reactions [1]. Characterization of relevant elements is laborious, and even intractable for soft actuators with many design parameters. This paper presents soft pneumatic actuator design characterization for actuation trajectories involving applications with external forces.

Researchers have explored modeling of hyperelastic silicone materials and their reactions to external forces [2], [3]. This has allowed others to characterize the response to external forces through analytical solutions [4] and energy methods [5], [6]. Energy methods allow general characterization but require solving sets of ordinary differential equations numerically, which is time-consuming and scales poorly during exploration of a parametric design space. For partially restrained (anisotropic) membranes, some have instead relied on simplified load estimation from contact-area assumptions [7]. Contact-based force transforms are valuable for their ease and speed of calculation, but their assumptions break down for larger actuators and strains. It is preferable to combine the strengths of both methods and fully characterize the actuators in the same manner that broader design spaces have been characterized for shape targeting without loading [8], [9].

We take inspiration from research that has used Kevlar strain limiters to reinforce and shape silicone membranes [10], [11]. Unlike the membranes discussed above, the trajectory of these Fiber-Reinforced Elastomeric Enclosure (FREE) is entirely defined by the inextensible deformation of the fiber elements. The design space for force application with single-expansion FREE's has been explored for slim cylindrical actuators with stiffer rubbers [12]–[14]. These slender actuators can struggle under compressive loading due to buckling [15], while wider-based balloons have been shown to be useful for lifting [7], [10], [16] and are less susceptible to catastrophic buckling due to their low slenderness and expanding cross-sectional area. Softer rubbers also allow the actuators in this work to operate at lower pressures with max pressures of 7.5 kPa.

Sequential experimentation and active learning provide a means of collecting new data to minimize overall error of a machine learning model [17]. Such models are able to provide accurate predictions at very fast speeds at inference time (forward pass on order of ms). Learning has been used for inverse design of shape response for strain-limited membranes [9], but data-driven methods of characterization have underperformed energy methods in the presence of external forces [13]. We aim to leverage active learning to explore the parameterized design space in a data-efficient way and reduce global model uncertainty. This will allow for designs targeted at specific lifting applications and reduced model error compared to theoretical, energy-based, methods.

In this work we characterize a parameterized class of actuator to design soft pneumatic actuators with optimized lift response. To understand the response of the inflated system, we solve energy minimization relations that estimate the inflated shape of the actuator in the presence of a known

Manuscript received: March, 31, 2025; Revised June, 30, 2025; Accepted August, 7, 2025.

This paper was recommended for publication by Editor Cecilia Laschi upon evaluation of the Associate Editor and Reviewers' comments.

[1]Department of Mechanical Engineering and Applied Mechanics (MEAM) at University of Pennsylvania, Philadelphia, PA USA gcampbel@seas.upenn.edu, yim@seas.upenn.edu

[3]Department of Physics at Syracuse University, Syracuse, NY USA

[3]Department of Mechanical Engineering at University of Wisconsin-Madison, Madison, WI USA

Digital Object Identifier (DOI): see top of this page

IEEE Robotics and Automation Letters (RA-L) paper, presented at ICRA 2026, Vienna, Austria. Cite as RA-L paper.

external force. We then use active learning to collect an efficient dataset that spans the prescribed parameter space and that includes strains beyond the linear-elastic region of elastomer deformation. We train our neural network model to interpolate and predict force response between collected data and design parameters. We prescribe a target lift (height and force) trajectory for a single pressure sweep and obtain an optimal membrane design as output. We demonstrate the utility of this model by using it to lift a mass along targeted trajectories as well as to maximize lift height.

II. Theoretical Actuator Modeling

A. Elastomeric Thin Membrane

We wish to determine the shape of a thin membrane upon inflation, with an external force applied at membrane radius, r, ranging from $0 \leq r \leq r_0$ as shown schematically in Fig. 1. Before deformation, the shape of the membrane that is not

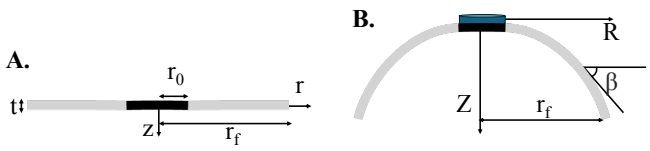

Fig. 1: Schematic of the membrane (gray) with strain limiter (black) in the A. undeformed state, and B. deformed state while in contact with external force (blue).

in contact with the force, using cylindrical coordinates, is given by $r_0 \leq r \leq r_f$, and membrane height $z = 0$. The region $0 \leq r \leq r_0$, which is in contact with the applied force, consists of low-strain material and we assume that there is no deformation in that region, only a translation of the region along the z direction. We assume the membrane stays axisymmetric after the deformation and its shape is given by,

$$R = R(r),\ Z = Z(r). \tag{1}$$

From this, we can write the deformation gradient as,

$$\mathbf{F} = R'(r)\hat{\mathbf{r}} \otimes \hat{\mathbf{r}} + (R(r)/r)\hat{\theta} \otimes \hat{\theta} + Z'(r)\hat{\mathbf{z}} \otimes \hat{\mathbf{r}}, \tag{2}$$

where primed variables indicate a derivative with respect to r. The eigenvalues of the right Cauchy-Green tensor, namely of $\mathbf{C} = \mathbf{F}^{\mathbf{T}}\mathbf{F}$, are the principal stretches of the membrane,

$$\lambda_1(r) = \sqrt{R'(r)^2 + Z'(r)^2},\ \lambda_2(r) = \frac{R(r)}{r}, \tag{3}$$

where $\lambda_1(r)$ represents the amount of material stretch along the meridian direction, while $\lambda_2(r)$ represents the amount of material stretch along the latitude direction. The third principal stretch comes from our assumption of incompressibility, $\lambda_1(r)\lambda_2(r)\lambda_3(r) = 1 \rightarrow \lambda_3(r) = 1/(\lambda_1(r)\lambda_2(r))$, where $\lambda_3(r)$ represents the material stretch in the direction normal to the membrane (thickness direction). We write an energy for the system that assumes full contact between the contact plate and the strain limiting contact region as shown in Fig. 2B.

$$E = \int_{r_0}^{r_f} \left(\underbrace{2\pi\, r\, t\, W(\lambda_1, \lambda_2) dr}_{\text{elastic energy}} - \underbrace{\pi\, pR^2\, Z' dr}_{\substack{\text{work done by} \\ \text{pressure difference}}} \right) + \int_0^{r_0} \left(\underbrace{-FZ' dr}_{\text{external force work}} + 2\pi\, r\, t\, \tilde{W}(\lambda_1, \lambda_2) dr - \pi\, pR^2\, Z' dr \right), \tag{4}$$

where W and $\tilde{W}$ are the strain energy per unit undeformed volume for the elastic material and the low-strain material respectively, while p is the gauge pressure inflating the membrane. In this study, we use the Gent model for the strain energy density function [18], which we can write as $W = -\frac{\mu J_m}{2} \ln(1 - \frac{\lambda_1(r)^2 + \lambda_2(r)^2 + \lambda_3(r)^2 - 3}{J_m})$. This model contains two constants, the shear modulus μ and the extension limit constant J_m. We find the elastic material constants using uniaxial testing, similar to [19]: $\mu = 31.7\ kPa$, $J_m = 39.6$. We estimate sufficiently stiff values for the strain limiting material based on data in [8]: $\tilde{\mu} = 1\ MPa$, and $\tilde{J_m} = 25$.

We first set the first variation of the energy to zero,

$$\delta E = \int_{r_0}^{r_f} D \left(\frac{\partial W}{\partial \lambda_1} \left(\frac{\partial \lambda_1}{\partial R'} \delta R' + \frac{\partial \lambda_1}{\partial Z'} \delta Z' \right) + \frac{\partial W}{\partial \lambda_2} \frac{\partial \lambda_2}{\partial R} \delta R \right) dr - \int_{r_0}^{r_f} \pi p \left(2RZ' \delta R + R^2 \delta Z' \right) dr - \int_0^{r_0} F \delta Z' = 0. \tag{5}$$

Where $D = 2\pi rt$. We then integrate, by parts where necessary, to obtain the equations of equilibrium and apply geometric relations based on $\beta(r)$, which we take to be the angle between the tangent to the membrane and the horizontal line at point r, as shown in Fig. 1B, $R'(r) = \lambda_1(r)\cos(\beta(r))$, $Z'(r) = \lambda_1(r)\sin(\beta(r))$. After simplification, we write the equilibrium equations for the $r_0 \leq r \leq r_f$ region as:

$$\frac{d\lambda_1}{dr} = \frac{W_2 - \lambda_1 W_{12}}{rW_{11}} \cos\beta + \frac{\lambda_2 W_{12} - W_1}{rW_{11}}, \tag{6}$$

$$\frac{d\lambda_2}{dr} = \frac{\lambda_1 \cos\beta - \lambda_2}{r}, \tag{7}$$

$$\frac{d\beta}{dr} = \frac{\tilde{p} r \lambda_1 \lambda_2 - W_2 \sin\beta}{rW_1}, \tag{8}$$

where $\tilde{p} = p/t$, $W_1 = \partial W/\partial \lambda_1$, $W_2 = W/\partial \lambda_2$, and $W_{12} = \partial^2 W/\partial \lambda_1 \lambda_2$.

The second term in Eq. 4 only contributes to the boundary conditions at r_0 since there is no deformation in the $0 \leq r < r_0$ region. The boundary conditions that come from the integration by parts give us a condition on the angle β, at $r = r_0$, so the initial boundary conditions needed to solve Eqns. (6), (7), and (8) are given by,

$$\lambda_1(r_0) = x; \lambda_2(r_0) = 1; \beta(r_0) = \text{ArcSin}\left(\frac{\pi p\, r_0^2 \lambda_2^2 - F}{2\pi t\, r_0 W_1} \right) \Big|_{r=r_0} \tag{9}$$

The condition on λ_2 comes from the fact that the contact area and the plate are in full contact and there is no extension in that area. The condition on β comes from the boundary

IEEE Robotics and Automation Letters (RA-L) paper, presented at ICRA 2026, Vienna, Austria. Cite as RA-L paper.

conditions obtained during energy minimization. We provide values for p and F, and solve the condition on λ_1 by using the shooting method to find the value of x that satisfies the condition $\lambda_2(r_f) = 1$. This final condition states that the membrane is fixed at the ends. Integrating the equilibrium equations from r_0 to r_f obtains the shape of the deformed membrane, and thus we find the height of the membrane for a given pressure and force value. Solving this relationship across many pressure-force pairings creates a theoretical model that can estimate forces for pressure-height pairings within, or nearby, the set.

B. Concentrically Strain Limited Thin Membrane

To span our actuator design space, we want to find the deformed shape of a membrane made up of elastic material that also includes strain limiting rings (see Fig. 2A). To do this, the energy in Eq. (4) will involve an extra integral for each additional piece we add to the system, with the strain energy density function W being used for the elastic material and $\tilde{W}$ being used for the strain limiting rings. We have to solve Eqns. (6), (7), and (8) for each of the material pieces separately, with the initial boundary conditions at each piece related through the boundary condition at the point of contact as well as the final boundary condition $\lambda_2(r_f) = 1$.

Solving this final boundary condition is unsuccessful, however, for 25% of membranes because of solver divergence brought on due to numerical stiffness for the heterogeneous material membranes. The successful subset of solutions are used and the results are discussed in Sec. IV-C.

III. Design space and experimental modeling

A. Design Space

While soft pneumatic actuators can take a large number of configurations, this work focuses on a class of soft pneumatic actuator defined as a thin (between 1 and 3 mm), circular membrane of radius 70 mm made from EcoFlex 00-30 rubber and reinforced with up to two axisymmetric rings (Soft n' Shear fabric). We ensure at least 10 mm between the outer and inner radius of a ring and contact areas between 25.4 and 38.1 mm. Our design space is an axisymmetric, finite, subset of all membrane-based SPA. An example membrane is seen in Figure 2A-B.

B. Data Collection

We fabricate membranes using gravity molding of Ecoflex 00-30. We apply lasercut strain limiting rings and contact regions (Soft n' Shear) to the uncured silicone after degassing and before curing. Membranes are mounted on a 3d-printed pressure chamber, which houses an air pressure sensor (MPRLS0025) and an ESP32 microcontroller to wirelessly transmit pressure data. Air pressure is supplied by a 4.5 V DC air pump (ZR370-02PM) and released by a 12V solenoid valve (Plum Garden). A piezoelectric load cell measures forces via an acrylic contact plate the same radius as the membrane's contact region and load is limited to move vertically with linear ball bearings.

We perform automated testing for each membrane where the contact plate is positioned vertically by linear actuators (Homend) and verified by a time-of-flight sensor (VL53L0X) between trials. A single trial consists of the activation of the pump and the subsequent inflation of the actuator. Inflation continues for ringed membranes until the internal gauge pressure reaches 4.3 kPa. Then the pump is deactivated and the solenoid valve releases air until internal pressure reaches atmospheric. If the membrane comes into contact with anything except the contact plate, the trial is completed. Three trials are performed per contact plate height, with eight heights, 0-70 mm, per membrane. If the membrane does not burst, testing is repeated to a maximum pressure of 6.1 kPa. Ringless membranes are given no pressure limit and allowed to inflate until contact with the test rig.

Data from each trial includes time, force, pressure, time of flight height, flow rate, contact with test rig (binary). Folder data includes material type, nominal thickness, radius, contact radius, test year, test month, test day, curing rack (A/B), contact plate nominal height, trial number, and ring data. While deflation data is recorded in some cases, exclusively inflation data is used in model training and verification. The data used in this study is also sorted into a learning-friendly format as a dictionary with key values matching membrane design parameters. This data, in the form of a .pkl file, can be found in the Github repository (see Data Availability section).

C. Model Architecture

Our neural network model predicts the external force $F \in \mathbb{R}$ generated by pneumatic membrane actuators under varying conditions. The model accepts three primary inputs: (1) a membrane design vector $M \in \mathbb{R}^6$ encoding six design parameters, (2) object displacement height $h \in \mathbb{R}$ from the actuator's initial plane, and (3) internal gauge pressure $p \in \mathbb{R}$. These inputs fully characterize the actuation task, allowing the model to interpolate between collected pressure-height-force data for tested membranes (Figure 2 D) and predict force responses for untested membrane designs.

The membrane design vector M encodes the following parameters: contact radius, membrane thickness, and four ring-related parameters (position and thickness for each of two potential rings, with NaN values indicating ring absence). Example vector formatting is shown in Table I.

Our approach follows the Operator Learning framework [20], [21], where neural networks operate on functions in potentially infinite-dimensional spaces. Specifically, given membrane design M and height h, our model outputs a function $F_{M,h} : \mathbb{R} \to \mathbb{R}$ that computes external force for any given pressure: $F_{M,h}(p)$ represents the force applied by membrane M at height h under pressure p.

Ring Encoder Design. To handle both ringed and ringless membrane designs within a unified architecture, we developed a specialized Ring Encoder that converts ring parameters (or their absence) into consistent latent representations. The encoder operates as follows:

- For valid ring parameters represented as $v \in \mathbb{R}^2$ (position and width), the encoder applies a linear transformation:

IEEE Robotics and Automation Letters (RA-L) paper, presented at ICRA 2026, Vienna, Austria. Cite as RA-L paper.

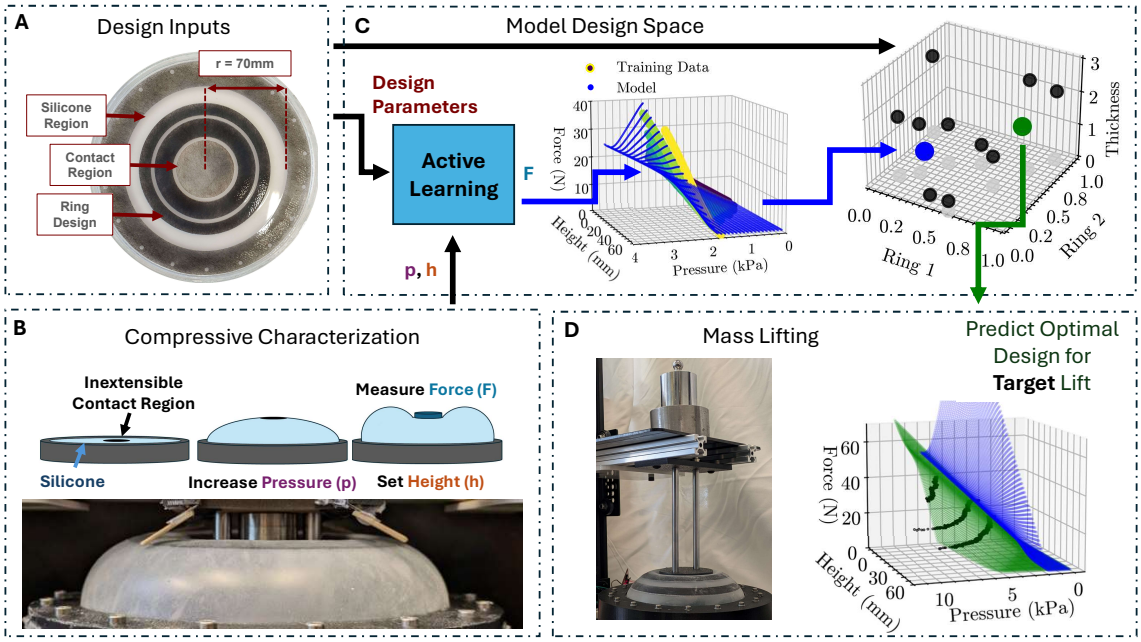

Fig. 2: A. Design parameters for example membrane. B. Compressive testing. (top) Testing procedure: expansion from a flat plane into a set height load-cell. Procedure is repeated for each membrane at different heights. (bottom) Example physical test measuring force for varying pressure at a set height. C. (left) Pressure, height, and six design parameters predict force output for a membrane. (middle) Model (blue) and force-pressure training data at varying heights (0-70mm from purple to yellow). (right) 3-D visualization of 6-D design space. Example training sets in black, model from C in blue, model from D in green. D. Optimization for lifting task. (left) Physical testing to verify lift trajectories at a given mass. (right) Model planes for (blue) training parameters and (green) design parameters optimized for target trajectories (trajectories in black).

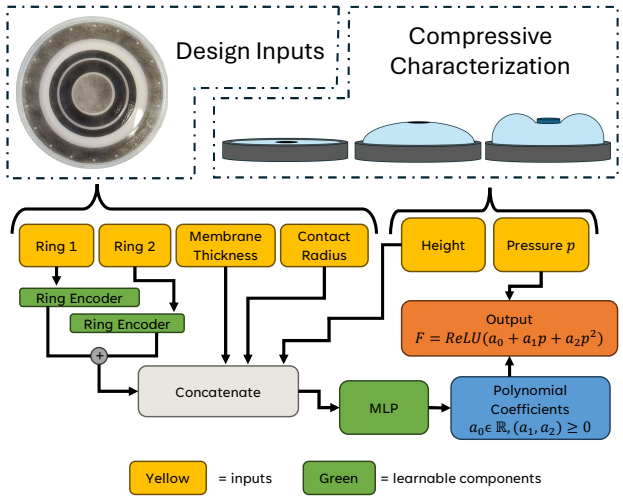

Fig. 3: Model Architecture. (Top) Characterization data, pressure and height, and design inputs, ring radius and width, membrane thickness, and contact radius, are inputs to the actuator model. (Bottom) The model solves for force output relative to pressure.

$e = Tv$, where $T \in \mathbb{R}^{d\times 2}$ is a trainable weight matrix projecting to dimension d.

- For missing rings (indicated by NaN), the encoder maps directly to a fixed but trainable vector $e_{NaN} \in \mathbb{R}^d$.

To ensure injectivity and prevent information loss, we set $d \geq 3$, leading e_{NaN} to lie outside the image of matrix T. We explored dimensions $d \in \{3, 12, 24\}$ during ablations, with a single shared architecture across all ring encoders to maintain consistent representations. The individual ring representations are summed, making the model invariant to ring ordering (Ring 1 vs. Ring 2) and adaptable for additional rings. The latent representation is passed into an initial MLP (we explored [layer, neuron] shapes of [8,8] and [16,5] during ablations) or passed directly into the base MLP.

Force-Pressure Relationship Modeling. The encoded ring information is concatenated with membrane thickness, contact radius, and height, then fed into a Multi-Layer Perceptron (MLP). This network computes polynomial coefficients that characterize the system's force-pressure response. Individual data-points are weighted during training such that each membrane test, not each data-point, contributes evenly.

We impose several physical constraints:

- *Monotonicity*: Coefficients multiplying pressure terms (a_1, a_2 for quadratic polynomials) are constrained to be non-negative (more pressure does not lead to less force).
- *Physical realism*: The constant term a_0 may be negative, but a ReLU activation is applied to the final polynomial output, preventing negative force predictions. That is, if at a given pressure the membrane is unable to lift the object, the model outputs 0 instead of a negative value. Although we do not directly enforce $a_0 < 0$, the

IEEE Robotics and Automation Letters (RA-L) paper, presented at ICRA 2026, Vienna, Austria. Cite as RA-L paper.

network successfully learns to predict this for every single membrane we tested.

During ablation studies, we evaluated MLP sizes ranging from 1 layer of width 8 neurons up to 4 layers each of width 64. For each MLP size we evaluated several function representations:

- Learnable basis functions (DeepONet strategy [21])
- Explicit polynomial assumptions (of degree 1,2,3).

The constrained polynomial representations (i.e. degree 2, shown in Fig. 3) proved superior, as the DeepONet formulation exhibited relative overfitting.

Training Details All networks were trained for 10,000 iterations using the Adam optimizer [22] on an Nvidia RTX A6000 GPU, requiring approximately 20 seconds per network during ablation experiments.

D. Active Learning

In order to carry out Active Learning (AL) [17], we must first be able to quantify the epistemic (model) uncertainty of our predictions under the operator learning framework [23]. We do this by using a Randomized Prior Network (RPN) ensemble of independent networks [24], [25]. Each of the $N \in \mathbb{N}$ members of the ensemble combines a prior and a trainable network to output a different prediction $F^1_{M,h}(p), F^2_{M,h}(p), \ldots, F^N_{M,h}(p)$, which are averaged in order to compute the final prediction $F_{M,h}(p) = \frac{1}{N}\sum_{i=1}^{N} F^i_{M,h}(p)$. The epistemic uncertainty is computed as the standard deviation of these predictions, with a small value indicating agreement between members of the ensemble (low epistemic uncertainty), and a large value indicating disagreement (high epistemic uncertainty). The active learning procedure is then carried out by selecting the membrane $M \in \mathbb{R}^6$ for which predictions on average have the highest possible value of epistemic uncertainty. Testing such a membrane and training the model with this newly acquired data then decreases the uncertainty for this membrane and other designs similar to it, since the model is now trained with the experiments from this specific design. We carry out this procedure iteratively, until enough membranes are acquired.

In particular, we carry out active learning in the parallel setting, where at each iteration $q = 2$ membranes are obtained simultaneously. We determine the best pair of membranes to collect by selecting designs that present largest uncertainty in predictions at selected heights $h_1, \ldots, h_{N_h}$ and pressures $p_1, \ldots, p_{N_p}$. This is quantified via the acquisition function

$$\alpha(M_1, M_2) = \sum_{l=1}^{N} \max_{k \in \{1,2\}} \left[\sqrt{\sum_i \sum_j \left(F_{M_k,h_i}(p_j) - F^l_{M_k,h_i}(p_j) \right)^2} \right] \tag{10}$$

which is maximized using the L-BFGS optimizer with several starting points, then taking the best optimized value overall. Note that the expression in Eqn. (10) is easily extendable to settings where we wish to collect an arbitrary number $q \in \mathbb{N}$ of membranes at each iteration, instead of only two.

IV. Results: Characterization & Modeling

A. Actuator Performance

The membranes central to these actuators use shore hardness 00-30 silicone rubber. This combined with the 70 mm actuator radius allows them to operate at pressures under 7.5 kPa and apply forces reaching 103 N. Maximum force occurred with a ringless membrane of thickness 2 mm and contact radius 38.1 mm at a height of 50 mm. We characterized each actuator's displacement up to 70 mm when possible, and heights up to 79 mm were reached during mass lifting. Without taking into account the membrane properties, the maximum contact area tested, 45.6 cm^2, would only be expected ($F = p * A$) to provide approximately 34 N of force.

We fabricated 28 different membranes, of which 22 were ultimately used in model training. Other membrane data was discarded primarily due to stiffening element delamination or development of a hole in the membrane. These modes of failure occurred exclusively at boundaries between unstiffened and stiffened regions of silicone. Fracture due to expansion past the rubber's strain limitation did not disqualify a membrane, though we removed the trial involving the fracture from that membrane's dataset. The resulting trimmed dataset included 188,318 individual data-points. Individual membrane designs each had between 1,906 and 17,044 data-points (median: 7,116, inter-quartile range: 4,583 to 12,780).

B. Model Performance (Ringless)

We compare the performance of the MLP-based pipeline to the theoretical (energy-minimization) model and a naive baseline regression. To create the second-degree polynomial baseline regression for ringed membranes, we concatenate all monomials up to order two for ring parameters, membrane thickness, contact radius, heights, and pressures. We fit a linear regression of this concatenation to the force outputs. We repeat these steps for a ringless membrane model, this time ignoring ring parameters in the concatenation.

We perform a $k = 3$ k-fold validation with pressure, height, and membrane design parameters as inputs and force as an output across the six ringless membranes. For each of the folds, we pick 2 membranes as our test set and use the remaining 4 for training, cycling through the groupings and taking the average test error across the 3 folds. Methods predicted force with the following root mean square error (RMSE): Neural Network (NN): 6.4 N, Theoretical model: 5.9 N, Regression baseline: 8.0 N. With the addition of the ringed data, the NN RMSE dropped to 5.1 N. The maximum force seen in the lift trials was 103 N, of which these RMSE represent between 5.0% (5.1 N) and 7.8% (8.0 N).

C. Model Performance (Ringed)

We optimize model hyper parameters for the entire dataset by sweeping: form of $F_{M,h} : \mathbb{R} \to \mathbb{R}$, width/depth of network, and latent ring representation. We compare the RMSE in model force relative to relevant test-set characterization data in a $k = 11$ k-fold cross-validation across 22 membranes.

IEEE Robotics and Automation Letters (RA-L) paper, presented at ICRA 2026, Vienna, Austria. Cite as RA-L paper.

The best-performing hyper-parameters result in a RMSE of 4.0 N (4% of max seen force) across ringed and ringless membranes. The model generally performs best with $F_{M,h}$ as polynomial degree 1, MLP depth of 3 or 4, and ring embedding model dimension of 12 or 24. MLP width doesn't have a large impact on result. Neither does the existence or parameters of a separate MLP for ring pre-processing.

It is difficult to baseline these values, as both the theoretical model and regression approach used for ringless trials fail to effectively deal with the parameterized ring values in all cases. Solving the theoretical model was successful for 75% of ringed membranes and the average RMSE across both ringed and ringless membranes was 4.4 N. The polynomial regression needed to be optimized separately with different numbers of input variables for ringed and ringless membranes, and the average RMSE across both sets was 9.4 N.

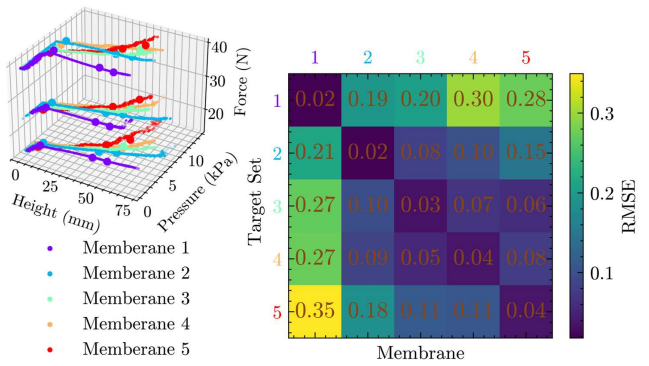

Fig. 4: (left) Pressure-height-force data from lifts at three different masses for each of five membranes (lines) with target points for each trajectory (circles). (right) RMSE between experimental trajectories and target way-points for each pairing of membrane and target.

V. Design for Open-Loop Applications

Once the NN model is trained, we use it to predict actuator performance in lifting tasks. We define a lift trajectory by the change in height of the object being lifted, the force applied by the actuator, and the pressure inflating the actuator. Our model therefore predicts the effect of design parameter choices on lift trajectories. Experimental lifts are performed with a 1 degree-of-freedom (DoF) test stage constrained by gantry plates. Masses are placed on the gantry and force is transmitted to the actuator via a contact plate (see Fig. 2.D).

We first verify model predictions on two membranes (one with and one without rings) from the training set. We model the expected lift trajectories for three target masses, 1.5kg, 2.5kg, and 4kg, and choose three points along each trajectory as target way-points. The points are chosen by the associated heights: 5, 40, and 50 mm. These heights were chosen because they represent areas of the trajectory that vary greatly between designs. We perform each lift and solve the error between the experimental trajectory and each way-point. Force is not included in this error metric because it is prescribed by the chosen mass. The total error between a membrane and the target points is defined as the root-mean square of the nine (3 mass x 3 way-point) errors:

$$RMSE = \sqrt{\frac{1}{n}\sum_{i}\left[\left(\frac{(p_{exp}-p_{target(i)})}{p_{max}}\right)^2+\left(\frac{(h_{exp}-h_{target(i)})}{h_{max}}\right)^2\right]} \quad (11)$$

where p_{max} and h_{max} are the limits of the space in which we model membrane forces: 10 kPa and 50 mm. p_{exp} and h_{exp} represent the respective pressure and height pair from the experimental trajectory that minimize the individual error.

The scaled RMSE for the in-set ringless and ringed membrane trajectories are both 0.02. We then designate trajectories for three membrane designs not in the training set. We choose these membranes specifically to span the pressure-height-force state space. We designate nine way-points for each membrane based on the model. We perform mass testing and error calculation as designated above. The scaled RMSE for these membranes are 0.03 to 0.04. Parameters for all five membranes are listed above the dashed line in Table I. Ring radius describes the radius at the center of the ring, ring width is the distance from that radius to the inner or outer radius ($r_{outer} - r_{inner} = 2 \cdot width$). For testing, the thickness values are restricted between 2.0 and 3.0 mm to minimize popping events. All other parameter ranges remain the same. The experimental trajectories and their target way-points are shown in Fig. 4. The associated errors are also shown in Fig. 4 - the main diagonal elements represents error along the trajectory for which each membrane was designed, off-diagonal elements represent each membrane's error related the the other membranes' trajectories. The decrease in error for a targeted membrane relative to the average of the other membranes' errors range from 69% to 93%.

TABLE I: Mass lift membrane design parameters [mm]

Thickness	Contact Radius	Ring_1 Radius	Ring_1 Width	Ring_2 Radius	Ring_2 Width
2.0	25.4	nan	nan	nan	nan
2.0	25.4	49.0	5.0	62.0	5.0
2.3	29.6	37.6	5.0	62.0	5.0
2.0	28.0	45.6	5.0	60.3	6.7
2.0	38.1	47.6	6.4	62.0	5.0
2.0	25.4	33.4	5.0	46.4	5.0
2.0	31.9	46.0	5.0	59.0	5.0

Using the inherent gradients and fast solve-time of the trained model, we are able to optimize for specific lift goals. As an example, we maximize lift height at given targets of pressure and force. We define the following posterior function Π: $\Pi = -k_{force} * F_{error} - k_{pressure} * p_{error} + k_{height} * h_{min}$ where k are scaling factors and h_{min} is the 'smooth min' score (via the LogSumExp operation of three height values). Local minima are found using gradient descent and compared across 2,500 random starting points. We choose two sets of target points, with forces across the three target masses (14.7

IEEE Robotics and Automation Letters (RA-L) paper, presented at ICRA 2026, Vienna, Austria. Cite as RA-L paper.

to 39.2 N). Target pressures are set at 6.9 kPa (set A) and 8.3 kPa (set B). The optimized parameters are listed below the dashed line in Table I.

We fabricate membranes based on the results of the optimization and test them as described for the five membranes above. We search the lift trajectories for points closest to the target force and pressure then record lift heights for each membrane at these points. A score is given based on the three heights, with a higher score matching a larger height. For each set of target points, the newest membranes had the highest score. Optimal membrane A reached a score of 29.4 for target set A. Among the five prior membranes, four reached all target points for set A and they averaged a score of 14.4. Optimal membrane B reached a height score of 40.8 for target set B. Two of the five prior membranes were able to reach the set B target pressure-force combinations, these two averaged a score of 25.7.

VI. Discussion

This paper uses a machine learning model to inform our design decisions within a parameterized design space for a force application task. We model the theoretical mechanisms governing the expansion of silicone-based SPA and develop a custom Neural Network (NN) architecture for exploring and quantifying the effects of the parameterized design space. The outputs of this model were verified and compared against two other types of models using a dataset gathered with automated experimentation. The trained model is used to define trajectory waypoints for membranes both in and out of the training set, confirmed with experimental mass lifts, and then to optimize for a specific lift output (maximize height).

The SPA we characterize in this study provide performance that could enable affordable means of force application for human motion. An actuator with the footprint of an adult head and a contact area smaller than an adult fist, backed by a 5 V battery and a portable air pump, is shown to provide forces over 100 N over a workspace of over 50 mm. Using just 22 membrane characterizations, we are able to train a model that provides 4.0 N RMSE across the entire parameterized design space. For a given force, we can design an actuator that will reach multiple points along a chosen pressure-height trajectory within approximately 4% error in height and pressure. These metrics indicate potential for performing premeditated lifting trajectories via a simple pressure sweep.

We can predict the way in which embedding concentric stiffening elements will alter the lift trajectory of a silicone membrane, proven by the small predicted error described in Section IV-C. It is important to contextualize the performance of our NN model with respect to state of the art theoretical models and off-the-shelf data-regression algorithms. We note that the simpler regression methods are not able to handle combined ringed and ringless data in the way that our NN model does. This and their large errors for ringed cases may indicate that they aren't a good choice for complex design parametrization. Similarly, the rigidity of the boundary condition on the energy minimization approach prevents its success in some ringed cases. Therefore for the ringed design space chosen for this work, the complexity of a NN appears to be warranted. Furthermore, once the NN model is trained, it is just as quick, if not quicker, to query as the other options.

When optimizing for lift height, parameters were often shifted to the edges of our design space. Specifically, the model recommended designs where the rings were as close as possible to either the contact area or the outer housing. Our manufacturing techniques don't allow for high precision in the placement of the rings, but automated methods might allow us to relax design parameter constraints. This would allow us to answer, for instance, what distance between rings maximizes lift height at different loadings.

Within the raw data we see the stiffening elements do not increase maximum force output or workspace of the actuators within the tested pressure range, and that they increase the relative pressure needed for a given force or height output. Adding more stiffening elements also increases the potential for membrane fracture due to increased boundary areas. Though neither was studied extensively in this work, this may decrease both the safe operating pressure for the membranes and their cycle life. While far more lift trajectories with ringed membranes are possible, a system designed using only ringless membranes may survive rougher usage.

Some of the most interesting performance within the collected dataset occur within unconstrained membranes. These membranes converge in pressure and force across different heights. This convergence is due to the hyperelastic constitutive relations of the silicone, and could be an important characteristic in lifting with this class of actuator. This convergence point also represents a difficulty for the theoretical model, and comparative error was higher at forces above it. This convergence, and the relatively higher forces per unit pressure from unconstrained membrane compared to strain limited membranes, both contributed to the higher model errors on this seemingly simpler subclass of actuator.

While the results of this particular membrane class are encouraging, the ability to effectively model any parameterized actuator class with a relatively small (n=22) dataset has wider implications within soft robotics. SPA researchers are using a variety of of multi-material designs to enable different interactions with the world. Active learning could help speed the exploration of these design spaces and lead to precisely tailored outputs. Offloading control complexity from the pneumatic input to the mechanical design can also enable us to move toward inexpensive and untethered robots that provide useful forces. We stopped characterization testing once our acquisition function started recommending 1-ring membrane designs, indicating that the 2-ring design space may be well characterized. There is likely still opportunity to decrease epistemic uncertainty further and in turn reduce NN model error, at the cost of additional testing.

VII. Conclusions & Future Work

We collect an active learning enabled n=22 dataset comparing force, height, and pressure across the design space for 70 mm radius concentric ring strain limited silicone soft pneumatic actuators. Actuators in this design space are found

IEEE Robotics and Automation Letters (RA-L) paper, presented at ICRA 2026, Vienna, Austria. Cite as RA-L paper.

to apply forces over 100 N and reach heights over 70 mm. This dataset trains an empirical model with less error than theoretical energy and naive regression models. The empirical model is fully differentiable, which we leverage for design optimization in a height-maximization mass lifting task.

While there is potential for these actuators to be useful individually given their high force and displacement outputs, we foresee more impact from their use in parallel. Because this model allows us to design for a given force/height pairing at a given pressure, we can connect multiple actuators to a single pressure source and prescribe their lift trajectories. If we can model the rigid body they are lifting, we can also model the kinematics of the lift from a single pressure source. Membranes displayed low hysteresis in our characterization testing, but additional work will be required to see what additional force-height-pressure planes can be reached once actuators are attached in parallel.

This model also allows for us to estimate the effect of (de)activating specific strain limiters, so long as the initial and final strain states remain in the design space. This, combined with variable limiters like those used in [16] could be used to alter lift trajectories for open- or closed-loop lifting.

While we consider the characterization data modeled in this study to be the most pertinent to soft pneumatic actuator lifting, there were additional datastreams recorded that are shared on Dryad, including volumetric flow and video of membrane expansion. We hope this data can be useful for better understanding the properties of inflated membranes undergoing concentric one-dimensional loading or as a comparison for improving analytical analyses. A possible future direction of research using this data is to develop a multi-fidelity model that leverages both experimental and analytical model data. Such a model could use large amounts of high-throughput theoretical data and calibrate predictions based on a small number of real-world experiments.

ACKNOWLEDGMENT

Thanks to Jason Matthew and R. Daelan Roosa for help in data collection. This work was supported in part by NSF EFRI award #1935294 and NSF NRT award #2152205.

DATA AVAILABILITY

The Python code and a .pkl file containing test data, is available on Github: https://github.com/gmcampbell/SPA_Design. The complete dataset, including tests not included in this paper and video of testing when applicable, is freely available on Dryad: https://doi.org/10.5061/dryad.jsxksn0mt.

REFERENCES

[1] A. D. Marchese, R. Tedrake, and D. Rus, "Dynamics and trajectory optimization for a soft spatial fluidic elastomer manipulator," *The International Journal of Robotics Research*, vol. 35, no. 8, pp. 1000–1019, 2016.

[2] W. Feng and W.-H. Yang, "On the contact problem of an inflated spherical nonlinear membrane," *Journal of Applied Mechanics*, 1973.

[3] W. W. Feng and H. Pangnan, "On the general contact problem of an inflated nonlinear plane membrane," *International Journal of Solids and Structures*, vol. 11, no. 4, pp. 437–448, 1975.

[4] X. Yang, L. Yu, and R. Long, "Contact mechanics of inflated circular membrane under large deformation: Analytical solutions," *International Journal of Solids and Structures*, vol. 233, p. 111 222, 2021.

[5] N. Herzig, J. Jones, E. Perez-Guagnelli, and D. D. Damian, "Model and validation of a highly extensible and tough actuator based on a ballooning membrane," in *2021 IEEE International Conference on Robotics and Automation (ICRA)*, IEEE, 2021, pp. 11 961–11 967.

[6] G. Shi, A. Shariati, J. Shi, N. Herzig, S.-A. Abad, and H. A. Wurdemann, "Modelling the inflation of an elastic membrane with a load," in *2023 IEEE International Conference on Soft Robotics (RoboSoft)*, IEEE, 2023, pp. 1–8.

[7] J. W. Ambrose, N. Z. R. Chiang, D. S. Y. Cheah, and C.-H. Yeow, "Compact multilayer extension actuators for reconfigurable soft robots," *Soft Robotics*, vol. 10, no. 2, pp. 301–313, 2023.

[8] J. Pikul, S. Li, H. Bai, R. Hanlon, I. Cohen, and R. Shepherd, "Stretchable surfaces with programmable 3d texture morphing for synthetic camouflaging skins," *Science*, vol. 358, no. 6360, pp. 210–214, 2017.

[9] A. E. Forte, P. Z. Hanakata, L. Jin, *et al.*, "Inverse design of inflatable soft membranes through machine learning," *Advanced Functional Materials*, vol. 32, no. 16, p. 2 111 610, 2022.

[10] N. Sholl, A. Moss, M. Krieg, and K. Mohseni, "Controlling the deformation space of soft membranes using fiber reinforcement," *The International Journal of Robotics Research*, vol. 40, no. 1, pp. 178–196, 2021.

[11] S. Ceron, I. Cohen, R. F. Shepherd, J. H. Pikul, and C. Harnett, "Fiber embroidery of self-sensing soft actuators," *Biomimetics*, vol. 3, no. 3, p. 24, 2018.

[12] F. Connolly, C. J. Walsh, and K. Bertoldi, "Automatic design of fiber-reinforced soft actuators for trajectory matching," *Proceedings of the National Academy of Sciences*, vol. 114, no. 1, pp. 51–56, 2017.

[13] A. Sedal, A. Wineman, R. B. Gillespie, and C. D. Remy, "Comparison and experimental validation of predictive models for soft, fiber-reinforced actuators," *The International Journal of Robotics Research*, vol. 40, no. 1, pp. 119–135, 2021.

[14] J. Bishop-Moser and S. Kota, "Design and modeling of generalized fiber-reinforced pneumatic soft actuators," *IEEE Transactions on Robotics*, vol. 31, no. 3, pp. 536–545, 2015.

[15] S. D. Thomalla, "High-force soft robots with applications in burrowing," Ph.D. dissertation, University of Minnesota, 2022.

[16] G. M. Campbell, J. Yin, Y. Song, U. Gandhi, M. Yim, and J. Pikul, "Electroadhesive clutches for programmable shape morphing of soft actuators," in *2022 IEEE/RSJ International Conference on Intelligent Robots and Systems (IROS)*, IEEE, 2022, pp. 11 594–11 599.

[17] P. Ren, Y. Xiao, X. Chang, *et al.*, "A survey of deep active learning," *ACM computing surveys (CSUR)*, vol. 54, no. 9, pp. 1–40, 2021.

[18] L. Zhou, S. Wang, L. Li, and Y. Fu, "An evaluation of the gent and gent-gent material models using inflation of a plane membrane," *International Journal of Mechanical Sciences*, vol. 146, pp. 39–48, 2018.

[19] L. Marechal, P. Balland, L. Lindenroth, F. Petrou, C. Kontovounisios, and F. Bello, "Towards a common framework and database of materials for soft robotics," *Soft Robotics*, 2020.

[20] Z. Li, N. Kovachki, K. Azizzadenesheli, *et al.*, "Fourier neural operator for parametric partial differential equations," *arXiv preprint arXiv:2010.08895*, 2020.

[21] L. Lu, P. Jin, G. Pang, Z. Zhang, and G. E. Karniadakis, "Learning nonlinear operators via deeponet based on the universal approximation theorem of operators," *Nature machine intelligence*, vol. 3, no. 3, pp. 218–229, 2021.

[22] D. P. Kingma and J. Ba, *Adam: A method for stochastic optimization*, 2017. arXiv: 1412.6980 [cs.LG]. [Online]. Available: https://arxiv.org/abs/1412.6980.

[23] L. F. Guilhoto and P. Perdikaris, "Composite bayesian optimization in function spaces using neon—neural epistemic operator networks," *Scientific Reports*, vol. 14, no. 1, p. 29 199, 2024.

[24] I. Osband, J. Aslanides, and A. Cassirer, "Randomized prior functions for deep reinforcement learning," *Advances in Neural Information Processing Systems*, vol. 31, 2018.

[25] Y. Yang, G. Kissas, and P. Perdikaris, "Scalable uncertainty quantification for deep operator networks using randomized priors," *Computer Methods in Applied Mechanics and Engineering*, vol. 399, p. 115 399, 2022.